Semi-Monolithic Meta-Scintillator Simulation Proof-of-Concept, Combining Accurate DOI and TOF

Georgios Konstantinou, *Member, IEEE*, Lei Zhang, Daniel Bonifacio, Riccardo Latella, Jose Maria Benlloch, Antonio J. Gonzalez, *Member, IEEE*, and Paul Lecoq, *Fellow, IEEE*

***Abstract*—In this study, we propose and examine a unique semimonolithic metascintillator (SMMS) detector design, where slow scintillators (BGO or LYSO) are split into thin slabs and read by an array of SiPM, offering depth-of-interaction (DOI) information. These are alternated with thin segmented fast scintillators (plastic EJ232 or EJ232Q), also read by single SiPMs, which provides pixel-level coincidence time resolution (CTR). The structure combines layers of slow scintillators of size 0.3×25.5×(15 or 24) mm^3 with fast scintillators of size 0.1×3.1×(15 or 24) mm^3. We use a Monte Carlo Gate simulation to gauge this novel semimonolithic detector's performance. We found that the time resolution of SMMS is comparable to pixelated metascintillator designs with the same materials. For example, a 15-mm deep LYSO-based SMMS yielded a CTR of 121 ps before applying timewalk correction (after correction, 107-ps CTR). The equivalent BGO-based SMMS presented a CTR of 241 ps, which is a 15% divergence from metascintillator pixel experimental findings from previous works. We also applied neural networks to the photon distributions and timestamps recorded at the SiPM array, following guidelines on semimonolithic detectors. This led to determining the DOI with less than 3-mm precision and a confidence level of 0.85 in the best case, plus more than 2 standard deviations accuracy in reconstructing energy sharing and interaction energy. In summary, neural network prediction capabilities outperform standard energy calculation methods or any analytical approach on energy sharing, thanks to the improved understanding of photon distribution.**

***Index Terms*—Depth of interaction, metascintillators, positron emission tomography (PET), scintillators, semi-monolithic, time of flight.**

I. Introduction

POSITRON emission tomography (PET) has reached a level of maturity as an imaging technique with the lancing of new scanners, such as the United Imaging total-body PET [1] and Siemens Quadra [2]. Current instrumentation developments mostly concentrate to enhance the overall sensitivity and signal-to-noise ratio (SNR) of the detector. Improved SNR directly translates to reduce examination time and radiation dose, improved image quality, or a combination of both. Apart from the improvement on subject coverage achieved with the aforementioned designs, there are three main directions to achieve this target.

The first corresponds to using scintillating materials with high-gamma stopping power, improving sensitivity through improving the number of recorded coincidences for a given amount of time and activity [3]. The second is related to improving the spatial resolution of the detector; this leads to higher granularity on detection and image through reduction of the transverse dimensions of the lines of response (LOR) [4]. To be noted, spatial resolution of the detector corresponds to the 3-D precision of gamma interaction localization, including both x–y coordinates and gamma depth-of-interaction (DOI), with the latter significantly affecting image quality away from the center of the field of view (FOV). The third direction reflects the improvement on image SNR by implementing time-of-flight (TOF) information on coincidences. There is a reverse square root relation between effective sensitivity and detector coincidence timing resolution (CTR) due to the segmentation of the LOR along its direction [5].

Further to these directions, combinatory improvements of detector specifications can provide synergistic added value to its effective sensitivity. As an example, we look in detail into the combination of DOI and TOF, which enhances detector effective sensitivity, through several mechanisms. On top of the TOF improvement, DOI adds the aforementioned reduction of LOR cross section, increases the number of LORs due to the addition of more resolvable detector elements, and finally reduces or eliminates the parallax error [6]. On top of

Manuscript received 24 April 2023; revised 3 August 2023 and 6 October 2023; accepted 14 October 2023. Date of publication 12 March 2024; date of current version 3 May 2024. This work was supported in part by the European Research Council in the framework of the ERC Advanced Grant TICAL under Grant 338953, and in part by the European Research Council (ERC) through the European Union's Horizon 2020 Research and Innovation Program (4D-PET) under Grant 695536. *(Georgios Konstantinou and Lei Zhang contributed equally to this work.) (Corresponding author: Georgios Konstantinou.)*

This work did not involve human subjects or animals in its research.

Georgios Konstantinou, Riccardo Latella, and Paul Lecoq are with Multiwave Metacrystal S.A., 1228 Geneva, Switzerland, and also with the Instituto de Instrumentación para Imagen Molecular, Centro Mixto CSIC, Universitat Politècnica de València, 46022 Valencia, Spain (e-mail: georgios@metacrystal.ch).

Lei Zhang is with Multiwave Metacrystal S.A., 1228 Geneva, Switzerland (e-mail: Lei@metacrystal.ch).

Daniel Bonifacio is with the Instituto de Pesquisas Energéticas e Nucleares, Cidade Universitária - bairro Butantã, São Paolo 05508000, Brazil.

Jose Maria Benlloch and Antonio J. Gonzalez are with the I3M, Centro Mixto CSIC, Universitat Politècnica de València, 46022 Valencia, Spain.

Color versions of one or more figures in this article are available at https://doi.org/10.1109/TRPMS.2024.3368802.

Digital Object Identifier 10.1109/TRPMS.2024.3368802

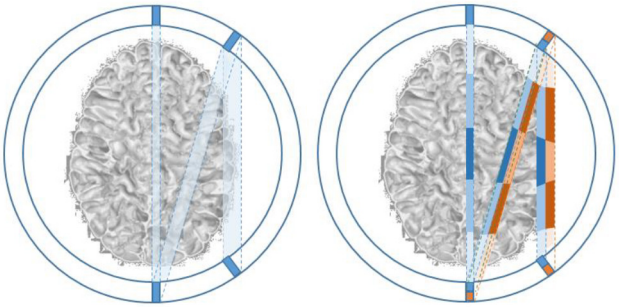

Fig. 1. Example of the added value when using DOI and TOF: Three simple LORs (left—light blue) are truncated transversely (light-blue and orange) due to DOI information and longitudinally with the use of TOF (variations of blue and orange), significantly improving the amount of information on the location of each annihilation, for each coincidence pair.

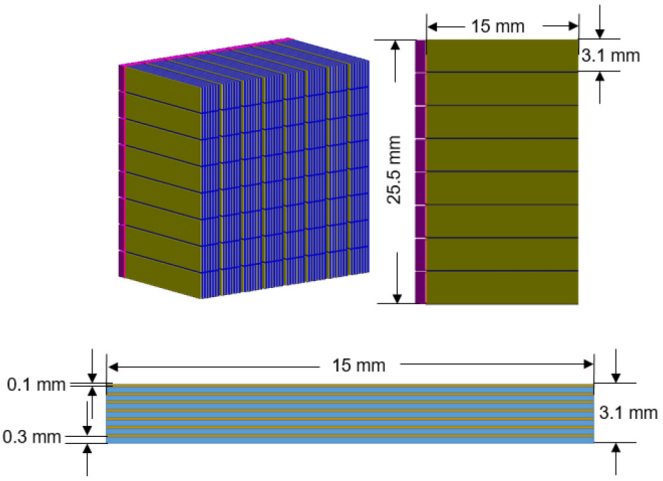

Fig. 2. Concept and simulation model of an 8×8 SiPM equivalent SMMS in orthographic (top left) and two side (top right, bottom) views: (gold) fast scintillator stripes 0.1×3.1×15.0 mm^3, (blue) 0.3×25.5×15.0-mm^3 slow scintillator semi-monolithic slabs, (magenda) optical grease, and (violet) SiPM. Projections are not in scale with each other, for reasons of clarity.

all these improvements, taking-into-account that DOI is the predominant mechanism deteriorating CTR for longer crystals, DOI knowledge allows mitigating this effect through a DOI-driven time-walk correction [7].

Parallax error can be particularly significant for architectures where FOV size is similar to the diameter of the object-of-interest, with main examples the designs of brain and preclinical PETs [4]. The same applies in other single organ architectures. Scanners with object-of-interest of up to 25 cm cannot easily apply TOF, as they would require detectors with coincidence time resolution (CTR) better than 400 ps for even a marginal TOF improvement; nevertheless, the development of cost-effective detectors capable of CTR around 200 ps and the expectation of system-level scalable designs in the near future [8] with timing close or better than 100 ps, brings the combination of DOI with TOF in the forefront of development of new PET designs. As an example, we showcase in Fig. 1 a human brain PET with 1.5-mm radial spatial resolution, only two DOI levels and 5 cm (330 ps) TOF resolution. For each coincidence, the SNR is improved by approximately 2 due to LOR lateral dimensions and another 2.5 times due to TOF.

One potential way to overcome the impasse between good timing and sufficient gamma absorption efficiency is the concept of metascintillators [5]. In the first generation, we combined a high-Z but slower compound, such as BGO or LYSO, with fast but light ones, such as BaF_2 and plastic. Herein, experimental results have shown agreement when compared to simulation. However, until now only pixel configurations having 1-to-1 matching between metascintillator and silicon photomultiplier (SiPM) have been tested. While timing is optimal under such conditions, there is no DOI information.

In this work, we present the simulated proof of concept of the added capabilities that the structuration of metascintillators can offer; through a design that slightly simplifies the metascintillating stack. Therefore, it is possible to reduce the amount of components to be included, with the further advantage of adding DOI capabilities. We use a novel, neural network (NN)-based approach to analyze event signatures and retrieve the maximum of information from several channels, while proposing ways to improve detector specifications with data driven corrections.

II. Materials and Methods

A. Semi-Monolithic Metascintillator Principle

A novel approach in achieving good DOI performance with good general detector characteristics is the semi-monolithic approach [9]. Herein, scintillators are cut in such dimensions as to be readable by a 1-D array of photosensors. Semi-monolithic, in this sense, corresponds to 1 lateral dimension being monolithic and 1 lateral dimension being pixelated.

The result of this is that the most of the photosensors of the 1-D array are illuminated for each event. The relative number of photons detected in each SiPM can be considered as a scintillation light distribution. The statistical characteristics of this distribution allows precise localization along the monolithic and DOI positions of the impinging event. The advantage of semi-monolithic designs is a better-event positioning than the pixelated, while having generally better timing than the monolithic.

This mechanism has been expanded to metascintillators. A potential design is to keep the semi-monolithic structure for the slow, high-Z component of the metascintillator. However, the fast material can remain segmented in the same dimensions as in pixelated designs. This means that the light from the slow material can be used to decode the y-z position of the impact position. However, the pixelated nature of the fast material allows fast photons to be contained in it and provide timing with the same availability as in the pixelated approaches. In this case, the semi-monolithic meta-scintillator (SMMS) is expected to combine monolithic capabilities of DOI, pixelated metascintillator quality TOF and sufficient stopping power (Fig. 2).

B. Computational and Simulation Concept

To test the aforementioned hypothesis, the Monte-Carlo platform GATE, based on GEANT4 was used [10]. An end-to-end pipeline was built, including three sequential steps: 1) data

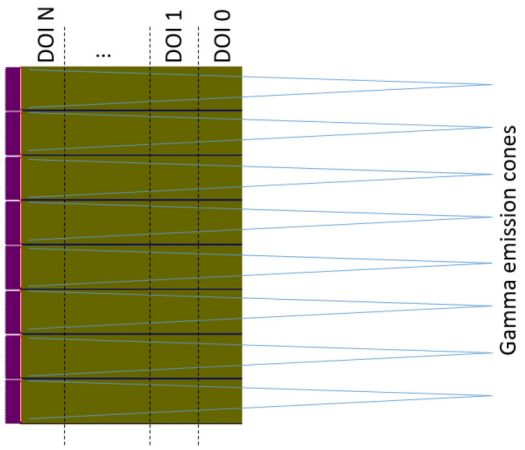

Fig. 3. Simplified sketch of the simulated architecture, side view. DOI levels are counted from the gamma emission direction inward. The gamma emission cones (blue lines) are not in scale.

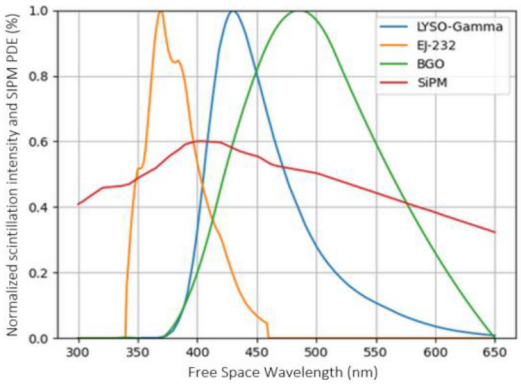

Fig. 4. Wavelength distribution of the model used for scintillator emission and SiPM PDE, as retrieved from corresponding sources (Saint-Gobain, Eljen, and FBK).

generation/collection; 2) data processing and preparation; and 3) model training and optimization. A python-based wrapper has been implemented to link the simulator, with a fully parameterizable set of variables customizing the geometry and materials of the simulated SMMS. This modular approach allows tests of different scenarios on the same raw or the same preprocessed data, without the requirement of rerunning the whole pipeline.

To reduce the computational complexity of the simulation, a single SMMS array coupled to 8 SiPMs was implemented. The resulting timing distributions correspond to detector time resolution (DTR) rather than coincidence time resolution (CTR); gammas are emitted at local time $t_0 = 0$. To compare the timing capabilities of SMMS based on pixelated approaches, the same simulation was made on a single metascintillator pixel. The calculation of the corresponding detector CTR, when two detectors of same DTR are placed in coincidence, is following the equation $\text{CTR} = \text{DTR} \times \sqrt{2}$ [5].

C. Simulator Characteristics

The array is irradiated from a distance of 50 mm, with a cone beam of 511-keV gammas that is wide enough to cover a 3×3-mm^2 section of the SMMS, roughly corresponding to the scintillating material over each SiPM. The beam is moved in 3-mm steps (Fig. 3).

The simulation includes both nuclear and optical packages. Cherenkov photon production has not been included. For the nuclear part, in order to perform a precise simulation of the energy sharing in the metascintillator, particle energy cuts were reduced to maximum convergence point, corresponding to 0.001 mm. For the optical part of the simulation, precise scintillation photon wavelength spectra were input, based on vendor-provided information [11], [12], [13], [14]. The wavelength distribution is of particular interest in the case of metascintillators, as they combine more than one material leading to a complex wavelength distribution, which interplays with the photon detection efficiency (PDE) distribution of the SiPM. Furthermore, optical grease and an absorption model of the photosensor was added. The SiPM considered the aforementioned wavelength-sensitive PDE (see Fig. 4), according to the specifications and size of FBK NUV, with 40-um SPAD size.

No special wrapping has been considered for the whole volume of the SMMS, meaning that the reflection/transmission behavior of optical photons will be following the Snell's law of idealized (polished) surface. The reflectance depends completely on the refractive index of corresponding materials. In these simulations, the refractive index of LYSO and BGO are set to 1.81 and 2.15, respectively. Finally, the coupling with photodetector is modeled by optical grease with refractive index of 1.5 and 0.1-mm thickness. The SiPM volume has been included but no material was assigned.

TABLE I
SMMS SIMULATED SCENARIOS

GEOMETRY SCENARIO	MATERIALS	LENGTH
BE15	BGO-EJ232	15 mm
LE15	LYSO:Ce-EJ232Q	15 mm
BE24	BGO-EJ232	24 mm
LE24	LYSO:Ce-EJ232Q	24 mm

D. Simulated Geometries

The simulated design was based on a realistic and possible to build combination of high-Z and fast materials, which leads to gamma sensitivity similar to the designs found in existing commercial systems. Layers of slow scintillator (BGO, LYSO) with sections coupled to the SiPM of 0.3×25.5-mm^2 and layers of fast scintillator (EJ232, EJ232Q-0.5% benzophenone) with areas of 0.1×3.1-mm^2 are used. These match the side dimension of 8 and 1 SiPM, respectively, including 0.1-mm space between them (Fig. 2). They are combined in structures of either 15-mm height, applicable for preclinical studies, or 24-mm height, relevant for clinical PET designs. Each SMMS of $\sim3\times25.5$-mm^2 area is externally wrapped with Teflon, modeled as such in GATE. The simulated geometries are listed in Table I. For clarity, different scenarios will be referred to through their material name from now on.

The two fast materials used differ in the quenching presence of benzophenone in EJ2332Q, which improves the timing

TABLE II
MATERIALS USED IN SIMULATION

MATERIAL	LIGHT YIELD	DECAY TIME
BGO	8400/MeV	300 ns
LYSO:Ce	32000/MeV	40 ns
EJ232	8400/MeV	1.6 ns
EJ232Q	2900/MeV	0.7 ns

characteristics of scintillation emission at the cost of a three-fold reduction of the light yield. More information on the materials used are listed in Table II.

An added element of these combinations is that they allow examination of extreme scenarios of energy sharing and measured energy correlation. The BGO-EJ232 produce almost the same light yield, meaning that separating the events that are fully absorbed in the system is possible through isolation of the photopeak. In contrast, LYSO:Ce and EJ232Q have almost an order of magnitude difference in their light yields, meaning that the final measured energy, corresponding to the effective number of photons produced, is strongly dependent on the energy sharing. This makes isolation of fully absorbed events significantly more complicated.

While the full waveforms of photon detection per SiPM are available, this analysis is focused on information which can be realistically retrieved in a scaled up system. The purpose for this is to demonstrate that energy sharing information is not carried only by more complex solutions (full waveform or waveform feature analysis), presented previously [15]. In this work we consider the total number of photons (TNP) and first photon arrival time (FPAT). These are surrogates of SiPM charge and a low-threshold timestamp, respectively.

To further expand the precision of the simulation, the single photon time resolution (SPTR) of the SiPM is added. This is given as a standard deviation value corresponding to the values found in literature [14]. While this is parameterizable, in the current modeling, a value of 70-ps full-width at half maximum (FWHM) (30-ps standard deviation) was used.

E. Post-Processing

GATE produces a vast list of information corresponding to every particle interaction, including the several thousand optical photons for each gamma event. In order to create an easy to use list of interactions, the majority of particles from the list is decimated, keeping only the information that is relevant to the particular experiment.

First, the spatial and temporal coordinates of the initial gamma interaction are recorded. Also, interactions concerning the extent of energy being absorbed by the scintillator are recorded in three categories: 1) scattered; 2) photoelectric; and 3) fully contained scattered. The last category corresponds to Compton scattering being the initial interaction, but with the process finishing with a photoelectric absorption at a different location of the scintillator. This is important as a secondary energy sharing mechanism, potentially producing errors concerning the initial location of interaction and accurate characterization of the LOR. Finally, the respective amount of energy deposition in the two materials is also stored for each event.

It has been demonstrated that significant information, such as the DOI, can be retrieved through the relative charges among the SiPM of a semi-monolithic array [9]. The respective timestamps are perhaps less useful in determining the DOI, but can be vital in calculating the extent of energy sharing. The mechanism of this corresponds to the 1-to-1 matching of fast material stripes to SiPMs, which leads to the produced prompt photons being recorded significantly earlier than those of the slow material which are distributed over the whole array.

F. NN Application

The main purpose of the structuration of SMMS is on retrieving DOI information from the distribution of optical photon detection, without compromising on the CTR. Based on the processed simulation results, we have first trained different machine learning models to predict the DOI.

Initially, we focused on BE15 and LE15 scenarios, using only number of photons information. The input of the model is a 1-D array containing 8 numerical entries. The output can be an integer value indicating the DOI category in case of a classification problem, or a real number representing the coordinate of gamma interaction along the crystal longitudinal direction in case of a regression problem. To choose a suitable machine learning model, the Pycaret Python library for model benchmarking and hyperparameters training was used [16]. We first compared the accuracy of different common classifiers, such as multiple layer perceptron (fully connected NN) [17], random forest classifier [18], and extreme gradient boosting [19]. When tested on data from BE15 and LE15 scenarios, the fully connected NN was the optimal strategy in all cases. Then, hyperparameters of previously obtained NN models were automatically tuned with Pycaret to achieve optimal prediction accuracy. Finally, the resulting NN model was reimplemented with the Tensorflow Python library for test and analysis [20]. In the case of classification, the average quality of prediction is calculated as the ratio of correctly predicted events over all events. The visual tool to facilitate understanding of the process is a confusion map of real versus predicted values. The regression problem can be considered as a classification with infinitesimal category size. Thus, the corresponding confusion map is a 2-D scatter plot of the true versus predicted values. Calculating the quality of prediction in these terms deviates slightly from the traditional approach of plotting, fitting a gaussian and providing a FWHM value as the figure of merit. For the results of NN prediction to be comparable with traditional scenarios, we set a threshold of 0.75 successful prediction. This corresponds directly to the FWHM of a Gaussian, where roughly 75% of its values are found within this width. At the same time, the precision of accuracy is found through the performance of the models in key parameter indicators (KPIs). In the case of DOI, such KPI can be the extent of improvement of DTR with the application of relevant time-walk corrections [7], or that of energy resolution [21], given that the causal relation between DOI accuracy and DTR or energy resolution is well established.

In a second phase, we first repeat the same model training and testing process on the datasets from BE24 and LE24 scenarios. Same as before, these models are expected to predict DOI. In addition to the 8 TNP, we also feed the 8 FPAT, one per SiPM for each gamma event. These additional features can improve the DOI prediction as there is a strong correlation between Gamma interaction position and optical photon traveling time. This task was focused on in BE24 and LE24 scenarios, due to the limited performance achieved with the approach followed for BE15 and LE15 scenarios. Furthermore, all simulation data are being used without consideration on the amount of data corresponding to each class. This was due to the significant number of classes and the limitation in data production. Nevertheless, it is expected from the exponential form of beer-lambert law [15], that the majority of events take place closer to the gamma receiving side (DOI layer 0), leading to an imbalanced dataset. A different approach corresponds to balancing training data, meaning that each class is represented by the same number of events. This is done by building a training dataset limited in size by the amount corresponding to the least populated class.

After the work on DOI estimation, two fully connected NN models have also been trained to predict the total energy deposited inside fast scintillation material (EJ232 or EJ232Q) and slow scintillation material (BGO or LYSO). This was recorded, including energy by primary gamma and secondary particles, for each event. Using this true, known value of energy sharing was useful to predict through the application of NN both energy sharing extent, as well as the energy of interaction. This second step of phase one applied only on crystals of BE24 and LE24 scenarios and considers simulation results of not only 511-keV events but also scattering, for both training and testing dataset. The approximation of energy deposition values can serve for 2 uses. First, the sum of both outputs gives total energy deposition, allowing to discriminate fully absorbed from scattered events, allowing safe allocation of a LOR at system level. Second, the proposition of energy deposition in fast and slow scintillation material provides the energy sharing ratio of metascintillator [5].

III. Results

A. Distribution of Photoelectric Events

In Fig. 5 the distribution of photoelectric events is shown for scenarios BE15 (top) and LE15 (bottom), and for different DOIs. This is presented as a function of the total number of detected photons (x axis) and 3-mm DOI (color code, 0 at gamma entry side). BE15 has a distribution with significant range between 750 and 1500 photons, for the same impinging energy (511 keV), around the photopeak at 1090 photons. There is also a minor shift in mean, depending on the DOI level, of the order of few tens of photons. LE15 has a range similar to previously simulated energy sharing distribution [5], with some events with significant energy in the fast material reaching down to one sixth of the maximum value of the histogram. Due to the higher-light yield in LYSO:Ce, there is a better resolution of the main peak. There is a slight variation in the mean for different DOI levels, up to 300 photons (5800 for DOI 0-6100 for DOI 4).

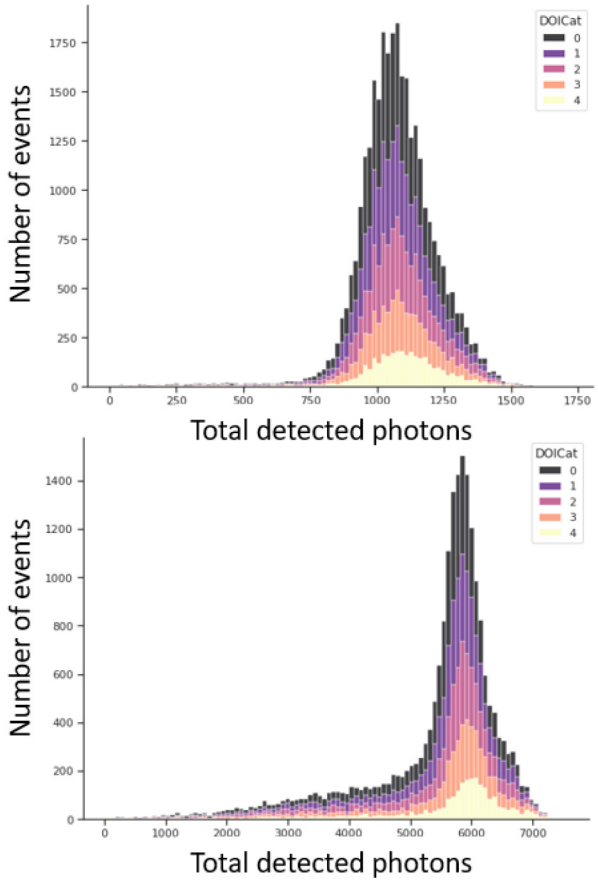

Fig. 5. Distribution of total detected photons for full absorption (511 keV) events in BE15 (top) and LE15 (bottom) scenarios.

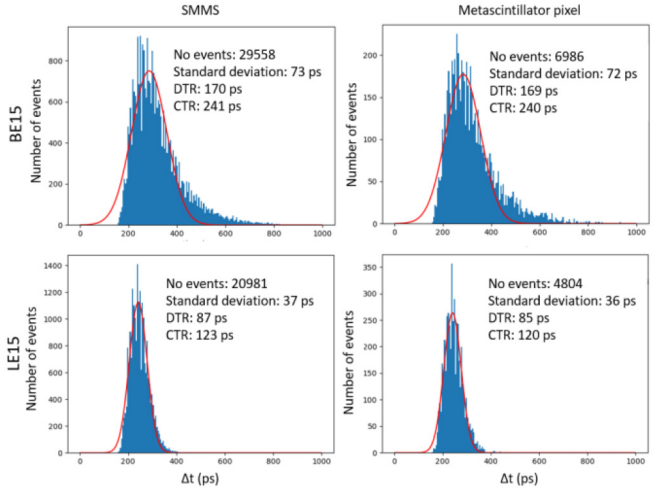

Fig. 6. (Top) BE15 scenario for SMMS (left) and pixelated (right) configurations; and (bottom) LE15 scenario for SMMS (left) and pixelated (right) configurations, distributions of FPAT, after SPTR blurring.

B. Comparison of DTR With Pixelated Detectors

In Fig. 6 a comparison of the timestamp distribution between the SMMS and fully pixelated metascintillators is

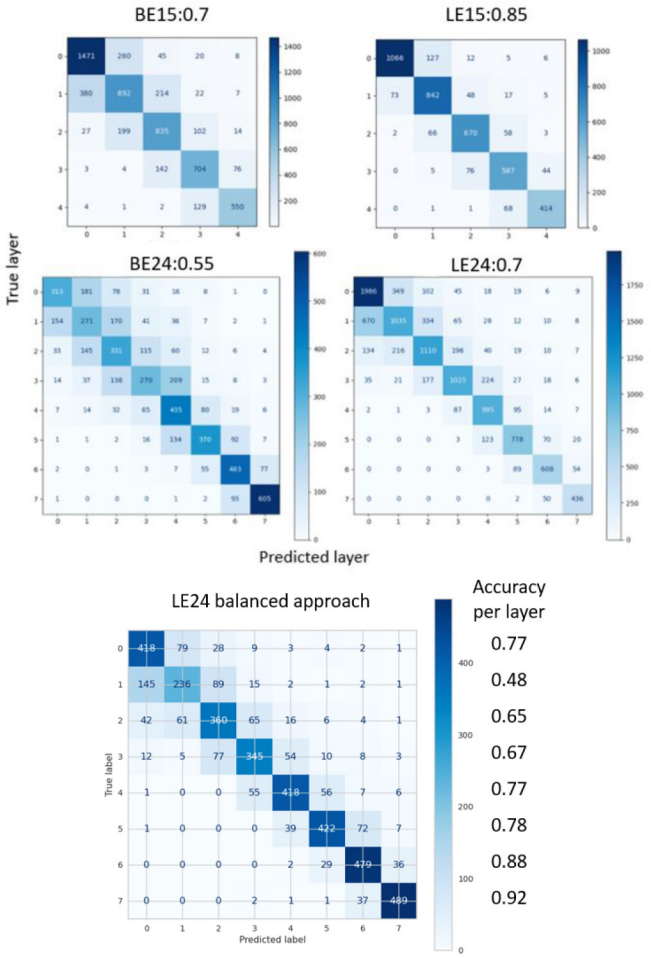

Fig. 7. (Top left) BE15, (top right) LE15, (middle left) BE24, and (middle right) LE24 confusion maps for 3-mm thick DOI layers; and (bottom) LE24 in balanced approach with overall precision 0.74. Variability in accuracy per layer can be observed in the list in right.

presented. This is simulation for same composition as BE15 and LE15. The difference in CTR-DTR is of the order of a couple of picoseconds, for both scenarios. Distribution and timing of BE15 is deviating ∼35 ps from the experimental results presented in [22] corresponding to ∼280 ps without timewalk correction, for a metascintillator pixel of the same characteristics.

C. DOI Classification Through NN

The applied fully interconnected NN was a simple unoptimized classifier model, with 8 inputs corresponding to the 8 SiPMs, one hidden layer of 150 perceptrons and outputs, corresponding to the number of DOI layers.

In a first attempt, DOI levels have 3-mm height, leading to 5 layers for BE15 and LE15 scenarios. The results are presented in Fig. 7 top and middle. For ∼10k events organized in a training (8432) and a testing set (2107), the average accuracy reaches 0.7 (BE15) and 0.85 (LE15), superior to that of FWHM in a Gaussian distribution (∼0.75). BE24 shows reduced average accuracy for 8 DOI layers of 3 mm each, rendering such DOI precision impossible (0.55). At the same time, LE24 is close to FWHM precision (0.7) and reached

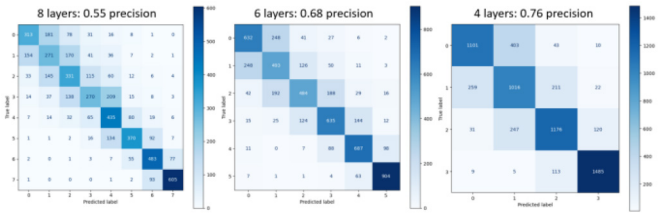

Fig. 8. BE24 for different DOI segmentations and precision: (Left) eight DOI layers of 3 mm, (middle) six DOI layers of 4 mm, and (right) four DOI layers of 6 mm. The last scenario reaches 0.76 precision.

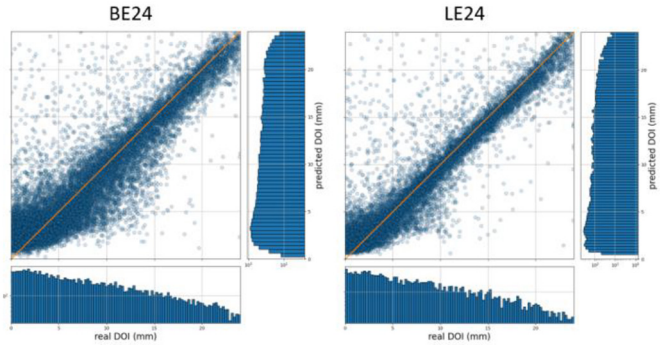

Fig. 9. Regression-based DOI prediction for BE24 and LE24 scenarios.

0.74 when the training dataset was switched to a balanced approach (Fig. 7). An important point when observing DOI classification results is that overall accuracy is not distributed equally over all classes. In particular, highest accuracy is found at the layers closer to the SiPM along with the most distant one. This is presented, in example, along with the confusion map of the balanced approach on LE24 scenario in Fig. 7 bottom.

This imbalance is caused by the photon dispersion within the semi-monolithic, which leads to photons in the intermediate but distant classes to have reduced accuracy, in contrast to the ones closer to the SiPM readout side (predominantly direct light), or the first one after gamma entry (back-reflected and direct light add up).

As the goal of classification quality equal to FWHM accuracy is far from reached for BE24, a study of different number of DOI layers was performed. In Fig. 8 the prediction accuracy for different DOI layers is presented.

D. DOI Regression Through NN

For comparison purposes, DOI was also approached through regression for BE24 and LE24 scenarios as presented in Fig. 9. As it can be observed, the variability of prediction accuracy depending on the DOI area persists in this approach as well, as prediction is significantly more accurate closer to the photosensor. A metric, similar to the average accuracy in the classification case is ineffective. This is because such metric does not represent the accuracy distribution through the length of the structure. For this reason, the KPI of DTR improvement through a DOI-driven timewalk correction has been used (Fig. 10).

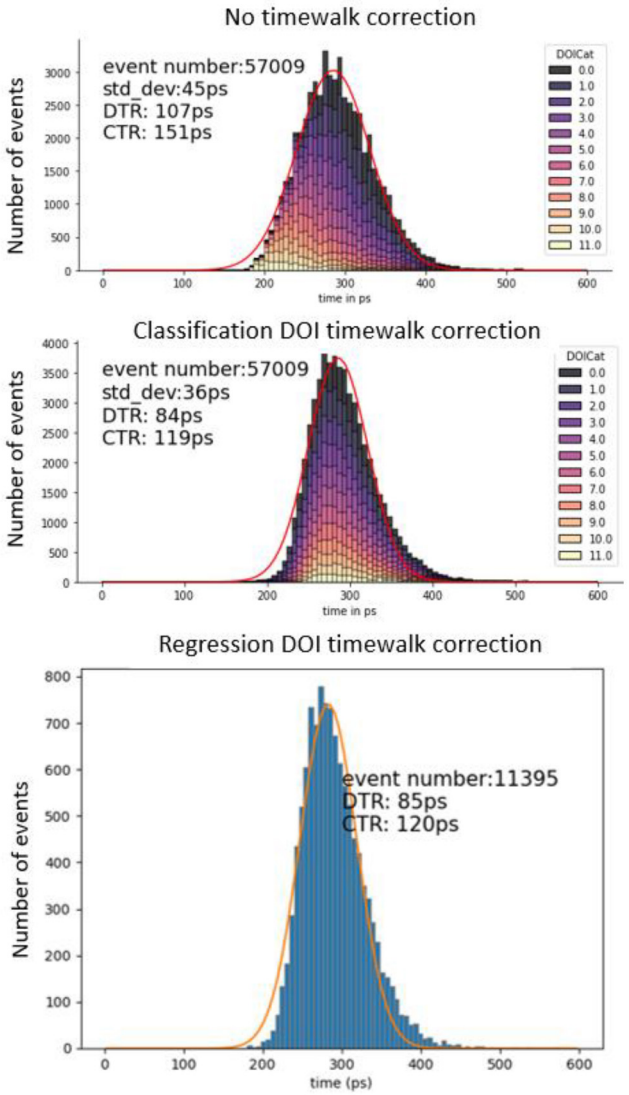

Fig. 10. DOI-driven timewalk corrections for a 3-mm classification (middle) and a regression (bottom) NN approach for LE24 scenario.

E. DOI-Driven Timewalk Correction

The synergy between TOF and DOI was investigated through a DOI-driven timewalk correction. The first approach was based on the classification results of the previous section. By plotting events according to their DOI, it is possible to observe the expected relation between DOI and photon detection time correction (Fig. 10 for LE24 scenario). This is further denoted by the mean value presented in the plot. By aligning these mean values, it is possible to produce a significantly improved DTR. A similar approach is used in the regression case. In particular, for LE24 scenario the calculated CTR value is 120 ps. The improvement through the application of DOI driven timewalk correction for all scenarios is presented in Table III. In the same figure a DOI-driven timewalk correction is also placed, based on the DOI prediction of a regression model. The KPI of DTR shows similar performance for both regression and classification NN approaches.

TABLE III
TIMEWALK CORRECTION FOR ALL SCENARIOS

SCENARIO	RAW DATA CTR	TIMEWALK CTR	IMPROVEMENT
BE15	244 ps	225 ps	8%
LE15	123 ps	107 ps	13%
BE24	292 ps	253 ps	13%
LE24	153 ps	120 ps	22%

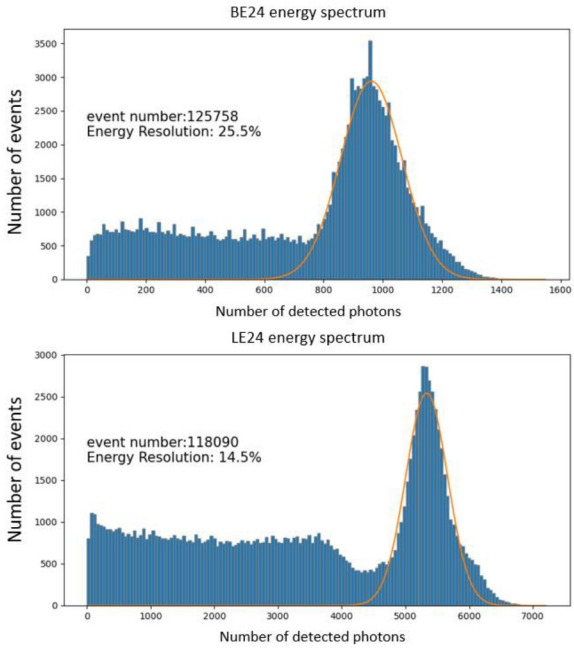

Fig. 11. Energy spectra for BE24 and LE24 scenarios at top and bottom respectively.

F. Energy Spectra

In Fig. 11 the energy spectra are presented for BE24 and LE24 scenarios. The corresponding energy resolution is 25.5% and 14.5%, respectively. Similar results are seen for BE15 and LE15 scenarios. To be noted that the second resolution corresponds to a feature similar to a photopeak, which however includes only events with none or only limited energy sharing. This can be better understood if this is compared with the spectra of Fig. 4. Full-absorption events with significant energy sharing have the same effective light yield as not-shared scattered ones.

G. Energy Sharing

Energy sharing was tackled in particular for BE24 (Fig. 12 top) and LE24 scenarios (Fig. 12 bottom), through the application of a regression NN model. The plots on the left correspond to histograms showing the deviation of prediction from the known value as a percentage of that value. The plots on the right correspond to scatter plots of real versus predicted values, demonstrating the distance from the mean (red line) which shows the correct prediction. The energy sharing resolutions are 16% and 9.5%, for BE24 and LE24 scenarios, respectively. These are significantly better that the calculated energy resolution in the previous section. This can be attributed to the

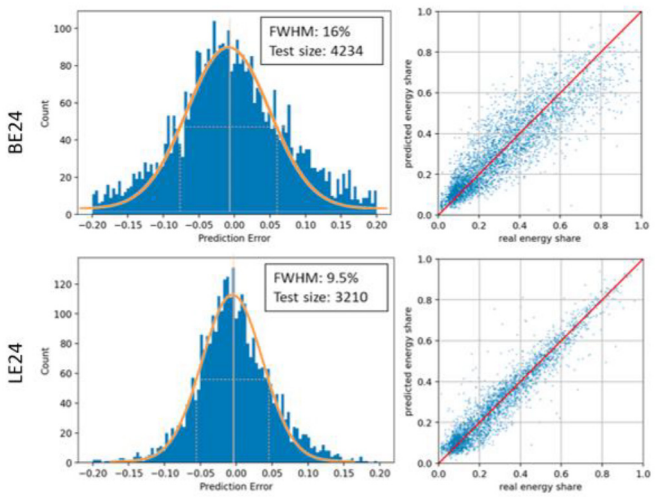

Fig. 12. Energy sharing for BE24 (top) and LE24 (bottom) scenarios: (Left) histograms of prediction error for all events and (right) scatter plots of real versus predicted energy sharing values.

TABLE IV
INTERACTION ENERGY-BASED EVENT CLASSIFICATION FOR BE24 SCENARIO

FILTER ENERGY	450 KEV	400 KEV	350 KEV
Correctly estimated fully absorbed	14947	15194	15390
Underestimated fully absorbed (%)	486 (3.1)	303 (1.9)	202 (1.3)
Overestimated scattered (%)	306 (2.9)	403 (3.9)	564 (5.5)
Correctly estimated scattered	10205	9958	9762
Overall precision	96.85%	97.19%	96.95%

fact the NN has access to not only the number of photons, but their spatial distribution with 3-mm transverse resolution. In this sense, the NN can provide more advanced mechanisms in estimating energy related quantities per event, than the simple addition corresponding to the traditional energy histogram as in Fig. 11. BE15 and LE15 scenarios have slightly improved results.

H. Reconstruction of Energy of Interaction

Since the classification of events as fully absorbed or scattered is very imbalanced, this problem was approached through a regression NN model. The results are presented in Fig. 13 left, presenting exponential scale histograms of real and predicted values along with the scatter plot, for BE24 scenario. This demonstrates that the question of energy of interaction can be confidently addressed with this application for a scenario where light yield of the composing metascintillator materials is approximately the same.

Based on such plots, event classification can be achieved with the use of energy thresholds. In Table IV this is presented for three such thresholds, namely, 350, 400, and 450 keV. These tables serve as confusion maps for this post-regression classification approach. A parameter to evaluate the overall

TABLE V
INTERACTION ENERGY-BASED EVENT CLASSIFICATION FOR LE24 SCENARIO

FILTER ENERGY	450 KEV	400 KEV	350 KEV
Correctly estimated fully absorbed	10680	11037	11320
Underestimated fully absorbed (%)	646 (5.7)	315 (2.7)	209 (1.8)
Overestimated scattered (%)	386 (2.9)	715 (5.4)	1011 (7.6)
Correctly estimated scattered	12938	12581	12298
Overall precision	95.73%	95.64%	94.83%

precision is the percentage of true over all events. This parameter reaches values above 95%, corresponding to 2 standard deviations.

The same approach has been undertaken for scenario LE24, where light yield of the composing materials is an order of magnitude different. Overall precision is similarly high as in scenario III, above 95% (Table V). The scatter plot of real versus predicted energy deposition values is shown in Fig. 13 right. Similar results of precision are seen for BE15 and LE15 scenarios.

IV. DISCUSSION—FUTURE PLANS

The work presented in this letter corresponds to an extended simulation study which was further improved during its development. The current version of the simulator can be considered a digital twin of the SMMS detector, as all significant phenomena of the detector, including SiPM and electronics, are well understood and included. Nevertheless, the simulator is only the training ground for better understanding and development of the scintillation process in the SMMS. Yet, we consider likely that the developed algorithms and prediction models will find good application in experimental results [23].

The SMMS is a novel and high-performance approach in block scintillator detectors, as it allows unprecedented insight in the spatial distribution of the scintillation event onset, without any mechanical features, such as for instance a pixelated multilayer stack [24] or subsurface laser engraving [25]. In contrast, the stack of different materials, fundamental in the concept of metascintillators, leads to improved timing and carries the synergistic advantage of providing DOI, as demonstrated by these simulations. This architecture is tested using commercially available plastic as the fast material, however the main purpose is to prepare the algorithmic development for the future physical development of 2nd and 3rd generation of metascintillators [26]. In that case, the fast material can be anything from wholly devices hyperbolic metamaterials to scintillating nanoplatelet-loaded plastic or photonic crystal slabs [27]. Whatever the new material to be used, the way to analyze events as presented in this work finds direct application. This sprouts from the fact that even for an order of magnitude difference in light yield, event separation in scattered or photoelectric and precise detection of energy sharing has been possible.

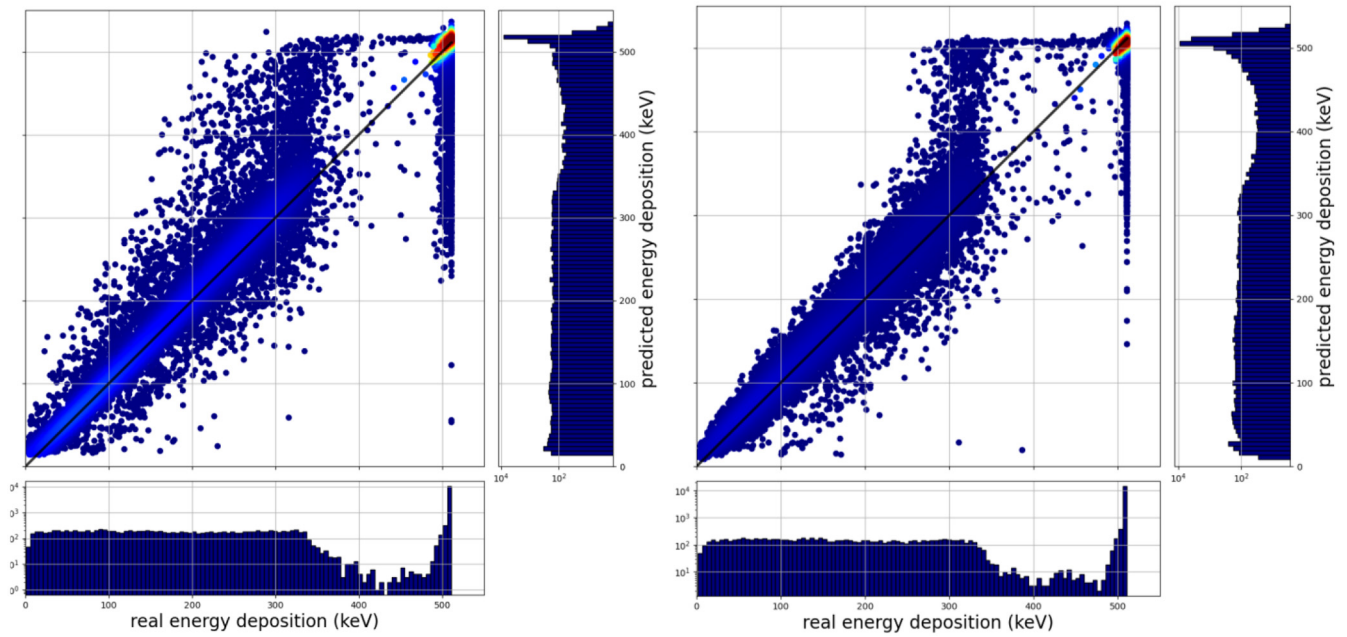

Fig. 13. Density color-coded scatter plot of energy deposition demonstrating the precision of prediction of the regression NN model, for BE24 scenario (left) and LE24 scenario (right). Bottom and right, corresponding real and predicted energy deposition histograms are presented in exponential scale.

The quest for optimized CTR has not been the focus of this work, as can be demonstrated by the lack of Cherenkov photon production in the used physics list. CTR optimization has been analytically researched in previous publications and is very much dependent on the matching between the scintillator structure and SiPM, read-out and data acquisition systems. Nevertheless, an effort has been made to demonstrate the increased synergy between DOI and CTR optimizations, by including an analysis on DOI-driven timewalk correction, which shows significant improvements of CTR up to 21%. A generalized framework on NN application is also unfortunately not possible, given again how the characteristics of the rest of the detector affect the information channels available. However, within the SMMS concept, work is ongoing to unify all timewalk corrections, including related with DOI, energy-sharing observed nonlinearity of the photon count with energy, into one generalized approach with focus on improved CTR. This will be presented in future publications.

While this model has strived to include as much information as possible, in order to present an accurate, configurable digital twin of the metascintillator detector, some aspects can still be improved. In particular, optical coupling between the material surfaces can be studied in more detail, to shed light on the amount of photons crossing between materials. This could affect the total light collection, due to absorption bands in different wavelengths. Similarly, more detailed refractive index and SiPM second order effects (cross-talk, SPAD dead time, dark counts) will be added in future versions of the simulator.

We have initially addressed the problem of DOI identification as a classification problem, in the intention to create clearly defined virtual detector elements of dimension $3\times3\times3$ mm^3. Such elements eliminate the parallax error and provide better-defined LORs, which significantly improve the spatial resolution of the whole system. Evaluation of this effect is ongoing within a framework of system level simulation with metascintillators [28]. However, an effort has also been made to address DOI identification as a regression problem, trying to define the exact DOI value. This approach is expected to optimize the dimensions of DOI to the minimum possible, while providing more precise values for the aforementioned timewalk correction. Moreover, DOI layers need not have the same size, but can be optimized to have dimensions above a certain confidence threshold, such as 0.75, equivalent to the FWHM of a gaussian distribution. Bigger or more balanced datasets could lead to improved results, while the possibility of predicting directly the virtual detector element, as an x–y–z space inside the SMMS, if enough data become available, is also expected to lead to a more precise model.

BGO-based systems seem to perform significantly worse than LYSO:Ce-based ones in relation with DOI classification and photon population evaluation (for instance Figs. 4, 6, 8 and 11). This issue is expected, given the generally lower-light yield of BGO which leads to reduced number of photons, along with its high-refractive index, which limits extraction. In a medium with the dimensions of the semi-monolithic plate, photons need to travel longer paths in the BGO until they are extracted, meaning that a significant number of these is absorbed. This variability leads to a significant spread and reduction of energy resolution, but also to reduced NN performance. Variable surface treatment and extraction facilitating media could improve this issue. Nevertheless, BGO remains an important material for metascintillators, due to the improved photoelectric cross section, ability to produce Cherenkov photons and lower-material cost, when compared with LYSO:Ce.

Using the same easily retrieved values of total charge and timestamp per SiPM, it has been possible to provide a significantly more accurate estimation of the extent of energy sharing. Most importantly, through this, it has been possible to provide a precise estimation of energy of interaction in complex metascintillators. This estimation is significantly better than the measured energy resolution provided from direct addition of the SiPM charges, as expressed in detected photon numbers. In this sense, this work opens the discussion on defining the classification of scattered and fully absorbed interactions as a percent quality score of a confusion map. In the specialized issue of PET LOR assignment, energy resolution becomes an obsolete metric, as the only interest in this case is to correctly classify events, something that is achieved significantly better with the application of NN. The same approach will be attempted in experimental measurements of SMMS. We believe that this improves the quality of the detector, through expanding the events amount that have been correctly characterized and thus improving detector sensitivity. Further to that, energy sharing definition allows for the isolation of ultrafast subsets, which can be used as priors for reconstruction in a multikernel approach. Work on this direction has also already started.

Using easily obtainable information allows for the NN approach to be generalized in preparation for application on full PET systems. In order to reduce the computational load, NN can be applied directly at the front-end, for instance within the data acquisition chain FPGAs [29]. Calibration runs can be programmed to take place periodically, to improve model quality through adaptation to exact acquisition conditions. In combination with metascintillator subset characterization, the traditional 1 to 1 detector coincidence, which was used for sinograms and reconstruction, is now becoming a complex vector which includes various kernels of timing along with several DOI levels. This computational upgrade can only be tackled, in order to allow fast acquisition and dynamic imaging, with specialized intelligence in the front-end detector. This challenge is necessary both for metascintillators and Cherenkov-driven event time tagging [30]. In this sense, the next step in order to bring system level capabilities to the new generation of detectors is to study and specialize the data acquisition system for metascintillator read-outs, both on ASIC and FPGA levels.

Metascintillator development is moving forward on several fronts: DAQ; scintillating component structuration; new scintillating materials; dedicated signal processing; and multikernel image reconstruction. With the presented framework we add an important stepping stone for the second (structuration) and fourth (signal processing) of these directions. To facilitate adoption of the metascintillator, or more generally, variable resolution scintillator paradigms, we intend to publish a library of modular and adaptable analytic and machine learning functions, specialized in the specifics of these detectors. We believe that on the way to 10-ps CTR resolution, there is no other viable alternative than combining all of the above. A new paradigm for PET detector, requires reimagining the whole PET image concept. The advantages have been well described in literature [8].

V. Conclusion

This work presents a simulation of a novel scintillator architecture, the semi-monolithic metascintillator. We prove that this configuration bridges the advantages of two worlds, combining DOI information from the semi-monolithic with pixel-like CTR. The simulation model's accuracy has been compared with experimental results of the same system, showing a less than 15% discrepancy. This model includes the whole physical process from the nuclear gamma interactions, recoil electron energy release, scintillation photon production and propagation and higher-order characteristics, such as PDE, SPTR, and realistic light wavelength sensitivity.

The use of NN has been generalized to address important event characteristics, such as DOI and energy sharing, which are significantly improving precision and effective sensitivity of the detector. These NN receive input quantities that are easily retrieved from system level detector deployment, such as the total charge and timestamp per SiPM. In this sense, this approach paves the way for experimental application of the developed NN models.

With the predictions retrieved with this simple and lightweight NN model and some analytic corrections, we achieve a 107-ps CTR and <3-mm DOI for an LYSO:Ce-EJ232Q SMMS of 15-mm length, applicable in small animal PET designs and 120 ps and same DOI for the same configuration but 24-mm long. The SMMS of BGO-EJ232 with the same dimensions leads to 225 and 253 ps, respectively.

Energy sharing is successfully predicted through NN, without requirements for any enhancement on the readout scheme, such as the ones, described in previous works. Precision of energy of interaction estimation exceeds 95%. The new approach is applicable for all energy sharing scenarios, including ones based on LYSO:Ce and fast emitters with significantly lower-light yield.

Acknowledgment

All authors declare that they have no known conflicts of interest in terms of competing financial interests or personal relationships that could have an influence or are relevant to the work reported in this letter.

References

[1] S. R. Cherry, T. Jones, J. S. Karp, J. Qi, W. W. Moses, and R. D. Badawi, "Total-body PET: Maximizing sensitivity to create new opportunities for clinical research and patient care," *J. Nuclear Med.*, vol. 59, no. 1, pp. 3–12, 2018.

[2] I. Alberts et al., "Clinical performance of long axial field of view PET/CT: A head-to-head intra-individual comparison of the biograph vision quadra with the biograph vision PET/CT," *Eur. J. Nuclear Med. Mol. Imag.*, vol. 48, no. 8, pp. 2395–2404, 2021.

[3] De E. Ponti et al., "Clinical application of a high-sensitivity BGO PET/CT scanner: Effects of acquisition protocols and reconstruction parameters on lesions quantification," *Curr. Radiopharm.*, vol. 15, no. 3, pp. 218–227, 2022.

[4] H. G. Kang et al., "Submillimeter resolution positron emission tomography for high-sensitivity mouse brain imaging," *J. Nuclear Med.*, vol. 64, no. 6, pp. 978–985, 2023.

[5] G. Konstantinou, P. Lecoq, J. M. Benlloch, and A. J. Gonzalez, "Metascintillators for ultrafast gamma detectors: A review of current state and future perspectives," *IEEE Trans. Radiat. Plasma Med. Sci.*, vol. 6, no. 1, pp. 5–15, Jan. 2022.

[6] Z. Wang et al., "High-resolution and high-sensitivity PET for quantitative molecular imaging of the monoaminergic nuclei: A GATE simulation study," *Med. Phys.*, vol. 49, no. 9, pp. 4430–4444, 2022.
[7] X. He, C. Trigila, G. Ariño-Estrada, and E. Roncali, "Potential of depth-of-interaction-based detection time correction in Cherenkov emitter crystals for TOF-PET," *IEEE Trans. Radiat. Plasma Med. Sci.*, vol. 7, no. 3, pp. 233–240, Mar. 2023.
[8] P. Lecoq et al., "Roadmap toward the 10 ps time-of-flight PET challenge," *Phys. Med. Biol.*, vol. 65, no. 21, 2020, Art. no. 21RM01.
[9] M. Freire et al., "Position estimation using neural networks in semi-monolithic PET detectors," *Phys. Med. Biol.*, vol. 67, no. 24, 2022, Art. no. 245011.
[10] S. Jan et al., "GATE: A simulation toolkit for PET and SPECT," *Phys. Med. Biol.*, vol. 49, no. 19, pp. 4543–4561, 2004.
[11] Retrieved 08.03.2023. [Online]. Available: https://www.crystals.saint-gobain.com/files/881/download
[12] Retrieved 08.03.2023. [Online]. Available: https://www.crystals.saint-gobain.com/files/571/view
[13] Retrieved 08.03.2023. [Online]. Available: https://eljentechnology.com/products/plastic-scintillators/ej-232-ej-232q
[14] A. Gola et al., "NUV-sensitive silicon photomultiplier technologies developed at Fondazione Bruno Kessler," *Sensors*, vol. 19, no. 2, p. 308, 2020.
[15] G. Konstantinou et al., "A proof of concept of cross-luminescent metascintillators: Testing results on a BGO: BaF2 metapixel," *Phys. Med. Biol.*, vol. 68, no. 2, 2023, Art. no. 25018.
[16] U. Gain and V. Hotti, "Low-code AutoML-augmented data pipeline—A review and experiments," *J. Phys., Conf. Ser.*, vol. 1828, no. 1, 2021, Art. no. 12015.
[17] U. Seiffert, "Multiple layer perceptron training using genetic algorithms," in *Proc. Eur. Symp. Artif. Neural Netw.*, 2001, pp. 159–164.
[18] M. Pal, "Random forest classifier for remote sensing classification," *Int. J. Remote Sens.*, vol. 26, no. 1, pp. 217–222, 2005.
[19] *XGBoost: Extreme Gradient Boosting; R Package Version 0.4-2 1.4*, XGBoost, Seattle, WA, USA, 2015.
[20] P. Singh and A. Manure, "Introduction to Tensorflow 2.0," in *Learn TensorFlow 2.0: Implement Machine Learning and Deep Learning Models With Python*. New York, NY, USA: Apress, 2020, pp. 1–24.
[21] Y. Li et al., "DOI correction for gamma ray energy reconstruction based on energy segment in 3D position-sensitive CdZnTe detectors," *J. Instrum.*, vol. 17, no. 3, 2022, Art. no. T03004.
[22] G. Konstantinou et al., "Metascintillator pulse feature and shape analysis to detect photoelectric interactions and energy sharing," in *Proc. IEEE Nuclear Sci. Symp. Med. Imag. Conf. (NSS/MIC)*, 2021, pp. 1–4.
[23] P. Carra et al., "A neural network-based algorithm for simultaneous event positioning and timestamping in monolithic scintillators," *Phys. Med. Biol.*, vol. 67, no. 13, 2022, Art. no. 135001.
[24] H. G. Kang et al., "Initial results of a mouse brain PET insert with a staggered 3-layer DOI detector," *Phys. Med. Biol.*, vol. 66, no. 21, 2021, Art. no. 215015.
[25] G. Konstantinou, R. Chil, M. Desco, and J. J. Vaquero, "Subsurface laser engraving techniques for scintillator crystals: Methods, applications, and advantages," *IEEE Trans. Radiat. Plasma Med. Sci.*, vol. 1, no. 5, pp. 377–384, Sep. 2017.
[26] G. Konstantinou, "Metascintillators for ultra-fast gamma detectors," in *Gamma Ray Spectroscopy*. Cham, Switzerland: Springer, 2023, pp. 209–230.
[27] R. M. Turtos et al., "On the use of CdSe scintillating nanoplatelets as time taggers for high-energy gamma detection," *Npj 2D Mater. Appl.*, vol. 3, p. 37, Oct. 2019, doi: 10.1038/s41699-019-0120-8.
[28] D. A. B. Bonifacio et al., "Analytical model for the sensitivity of a cylindrical PET system based on bulk materials or metascintillators," *IEEE Trans. Radiat. Plasma Med. Sci.*, to be published.
[29] F. Mueller, S. Naunheim, Y. Kuhl, D. Schug, T. Solf, and V. Schulz, "A semi-monolithic detector providing intrinsic DOI-encoding and sub-200 ps CRT TOF-capabilities for clinical PET applications," *Med. Phys.*, vol. 49, no. 12, pp. 7469–7488, 2022.
[30] N. Kratochwil, E. Auffray, and S. Gundacker, "Exploring Cherenkov emission of BGO for TOF-PET," *IEEE Trans. Radiat. Plasma Med. Sci.*, vol. 5, no. 5, pp. 619–629, Sep. 2021.